Phase synchronization and intermittent behavior in healthy and Alzheimer-affected human-brain-based neural network

R. C. Budzinski,[1] B. R. R. Boaretto,[1] T. L. Prado,[2] and S. R. Lopes[1,*]

[1]*Departamento de Física, Universidade Federal do Paraná, 81531–980, Curitiba, PR, Brazil*

[2]*Instituto de Engenharia, Ciência e Tecnologia, Universidade Federal dos Vales do Jequitinhonha e Mucuri, 39440–000 Janaúba, MG, Brazil*

We study the dynamical propieties of phase synchronization and intermittent behavior of neural systems using a network of networks structure based on an experimentally obtained human connectome for healthy and Alzheimer-affected brains. We consider a network composed of 78 neural subareas (subnetworks) coupled with a mean-field potential scheme. Each subnetwork is characterized by a small-world topology, composed of 250 bursting neurons simulated through a Rulkov model. Using the Kuramoto order parameter we demonstrate that healthy and Alzheimer-affected brains display distinct phase synchronization and intermittence properties as a function of internal and external coupling strengths. In general, for the healthy case, each subnetwork develops a substantial level of internal synchronization before a global stable phase-synchronization state has been established. For the unhealthy case, despite the similar internal subnetwork synchronization levels, we identify higher levels of global phase synchronization occurring even for relatively small internal and external coupling. Using recurrence quantification analysis, namely the determinism of the mean-field potential, we identify regions where the healthy and unhealthy networks depict nonstationary behavior, but the results denounce the presence of a larger region or intermittent dynamics for the case of Alzheimer-affected networks. A possible theoretical explanation based on two locally stable but globally unstable states is discussed.

I. INTRODUCTION

Neural systems are characterized by the presence of neural cells and a complex structure of connections among them [1]. A large variety of neural systems is found in nature, from those composed of just hundreds of neurons and a few thousand connections, as in the *Caenorhabditis elegans* nematode neural network [2], to large structures, e.g., the human brain, where $\sim 10^{11}$ neural cells and $\sim 10^{15}$ connections are found [3]. In general, the neural systems are composed of different subsystems (network areas), each one responsible for essential functions, e.g., language, memory and perception, vital regulations and more [1], each area preserving its own complex pattern of connectivity, making each one distinguishable from the others [4].

To mimic some characteristics of real neural systems and their complex connectivity patterns, the study of complex networks and networks of networks is particularly useful. The neural networks can be understood as a first approach to the real neural system, where neurons and connections are represented by nodes and links. Such a modeling of the neural system through a complex network can also be understood at a macroscopic level, where each neural area is represented by an entire network connected externally to other networks, and internally where the neurons are connected to other neurons of the same network. In general, different internal and external connection schema are considered [3,5–7]. The study of complex network phenomenology provides useful

approaches to many problems of science, mainly physics, chemistry, biology, physiology, and even social science [8–11]. An important phenomenon of complex networks consists of emergent behavior, where the collective dynamics is richer than the single sum of individual behaviors [10], resulting in a richness of dynamical properties such as phase synchronization, nonmonotonous (anomalous) synchronization processes, and nonstationary transitions to phase-synchronized states [12–16].

In this paper, we study a neural system composed of a network of networks. We consider 78 subnetworks, each one containing 250 neurons, resulting in a total of 19 500 neurons in the entire system. The use of subnetworks brings the possibility to distinguish different network areas, allowing some heterogeneity for the entire network. The connection architecture between subnetworks is based on the connectome of the human brain obtained from the original work of Lo *et al.* [17]. The connectome is constructed using diffusion-weighted images [18] obtained from magnetic resonance data of 25 Alzheimer patients and a healthy control group composed of 30 cognitively normal, free of neurological disease, patients. The experimental procedure results in a weighted 78×78 matrix. The weight of each matrix element (i, j) depends on the number of fibers connecting i and j areas, determined using the fiber assignment with continuous tracking algorithm [19]. This reflects in some sense the observation that Alzheimer's disease can promote effects on the network level, affecting its dynamics [20–22]. The weight matrices are representative of a mean real topology of Alzheimer-affected and healthy brains. Differences on the distribution of the connections (fibers) between areas composing the neural system

*lopes@fisica.ufpr.br

in the disease and healthy cases are observed: Both follow a small-world topology but the Alzheimer-affected networks exhibit higher shortest path lengths [17], evidencing the loss of connections between brain areas and, consequently, loss of communication between different functional brain regions that reflects the cognitive decline in Alzheimer's disease. These points reveal the relevance of regarding dementia as a functional network disorder [22].

For each subnetwork, we consider a small-world topology coupling scheme, with a second neighborhood local structure, resulting in 1000 local connections added to ≈214 nonlocal connections (Newman-Watts route) [23], leading to 78 non-identical matrices with a similar small-world topology. The internal small-world topology is chosen since it adequately mimics real neural network connections by displaying high clustering and low average path length, two well-known characteristics of a small-world topology [2,24,25]. At the same time, the small-world coupling scheme shows rich dynamic behavior at the transition from unsynchronized to synchronized states [5,13,26,27] and may be useful to understand details of the not completely understood dynamics at the transition to globally stable synchronized states as the coupling strength is varied [28].

A network of networks, as supposed here, is also used in experimental situations where individual brain areas have been reported as statistically independent dynamical systems but depicting coherent behavior with other areas [29,30]. The transition to synchronization or collective coherent behavior in a neural network consists of a very important research point since there are indications of a close relation between excess (or lack) of synchronization levels of some neural diseases [31,32]. Some neurological disorders are also related to intermittent and nonstationary behavior of the brain dynamics [33].

The phase synchronization of a network is characterized by the temporal synchrony of the slow timescale of the neurons in the network. In order to quantify the phase synchronization, we compute the Kuramoto order parameter [34] based on data from the associated phase of each neuron. If the system displays a phase synchronization, then the order parameter gets close to 1, oscillating near a vanishing value for a nonsynchronized network.

To analyze the intermittent characteristics of the system, we make use of the recurrence quantification analysis, particularly the determinism (Δ) [35,36]. The δ analysis presents robust results to investigate the intermittent behavior [37] and can be evaluated making use of the mean field of the network only, as they are data that are experimentally obtained more easily [13,14].

The paper is divided as follows: In Sec. II the Rulkov model is presented and the internal and external connection schemes are defined. In Sec. III the associated phase of each neuron and the Kuramoto order parameter are defined and the recurrence matrix and the determinism are explained in detail. In Sec. IV results and discussions are shown, supporting the conclusions that are in Sec. V.

II. RULKOV MODEL AND CONNECTION ARCHITECTURE

Based on previous results [6,12–16], where distinct models lead to similar transitions to phase synchronization, we use
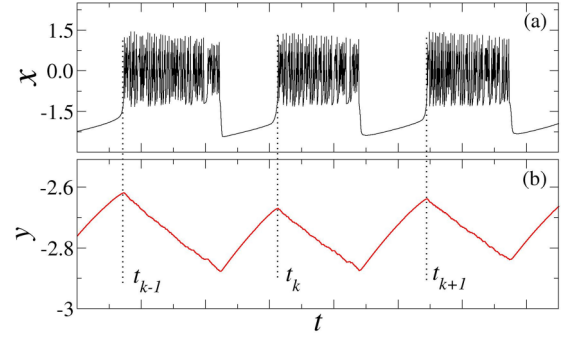

FIG. 1. Dynamical behavior of (a) fast x and (b) slow y variables of the neuron model, Eqs. (1) and (2). The fast variable (a) simulates the bursting neural activity, consisting of a sequence of chaotic spikes followed by a resting period, while the slow variable (b) is used to associate a geometric phase to each neuron since local maxima of y coincide temporally with bursting beginnings.

the Rulkov model [38], consisting of two coupled maps to reproduce the neuron behavior,

$$x_{t+1,i}^j = \frac{\alpha_i^j}{1 + \left(x_{t,i}^j\right)^2} + y_{t,i}^j + I_{\text{int},t,i}^j + I_{\text{ext},t}^j, \qquad (1)$$

$$y_{t+1,i}^j = y_{t,i}^j - 0.001 x_{t,i}^j + 0.001. \qquad (2)$$

Here $i = 1, \ldots, N$, where $N = 250$ is the number of neurons in each subnetwork; $j = 1, \ldots, M$, where $M = 78$ is the number of subnetworks; $x_{t,i}^j$ represents the fast variable of the system and can be understood as the membrane potential of neurons; and $y_{t,i}^j$ represents the slow variable of the system. The constant values were chosen in order to obtain the bursting behavior regime, as observed in Ref. [39]. We consider nonidentical bursting neurons characterized by the presence of two timescales: a fast one, related to the time interval between two chaotic spikes, and a slow one, consisting of the time interval of a sequence of spikes (a burst) followed by a quiescent period [40–43]. The distinction among neurons is made by the parameter α_i^j, randomly (Gaussian) distributed in the interval [4.15; 4.25] with a standard deviation of 0.02 and leading to bursting behavior for all neurons [39]. The typical fast-scale dynamical behavior of the neurons $x_{t+1,i}^j$ is depicted in Fig. 1(a), where bursts and quiescent periods are clearly visualized. Figure 1(b) depicts the slow variable $y_{t+1,i}^j$, making clear its relation with starting and ending of a burst.

The internal coupling term (I_{int}) between neurons in a subnetwork is

$$I_{\text{int},t,i}^j = \frac{\varepsilon_{\text{int}}}{\chi} \sum_{k=1}^{N} e_{i,k} x_{t,k}^j, \qquad (3)$$

where ε_{int} is the internal coupling strength, χ is the normalization factor given by the average number of connections in the network, and $e_{i,k}$ are small-world matrix elements. Each subnetwork has a nonidentical, but similar, small-world coupling matrix, resulting in a unique $\chi \approx 4.85$ value valid for all subnetworks.
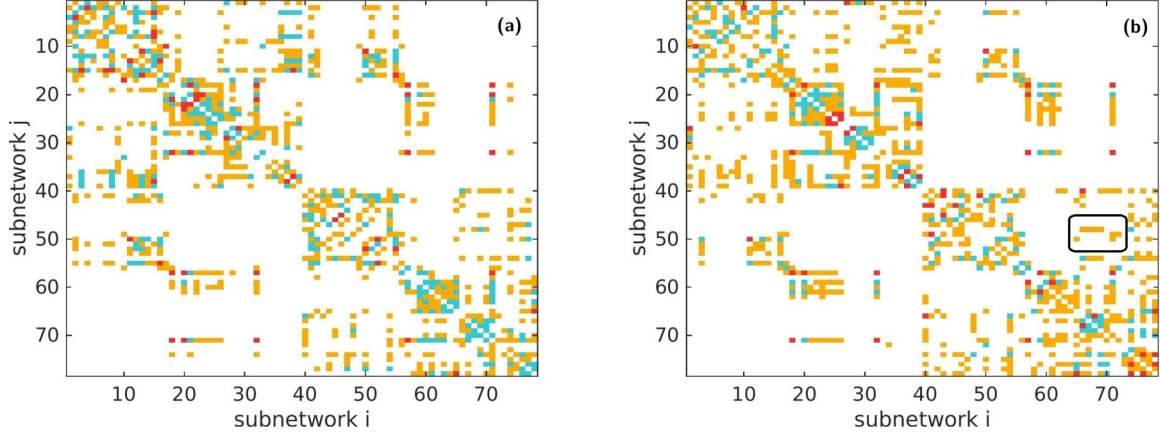
FIG. 2. Graphical representations of two examples of the human connectome where 78 neural subareas are identified. The matrices are obtained from magnetic resonance data of cognitively normal and Alzheimer patients [17] and rescaled into four discrete levels in Ref. [5]. Panel (a) and (b) show one example of a healthy and Alzheimer connective matrices. Four connection levels are identified for the case of healthy and Alzheimer-affected brains. A white pixel denotes the absence of connection, while yellow, blue, red pixels identify connection levels of intensity 1, 2, and 3, respectively.

The external coupling term (I_{ext}) is based on the human brain matrix given by

$$I_{\text{ext},t}^j = \varepsilon_{\text{ext}} \sum_{k=1}^{M} g^{j,k} \overline{V}_t^k, \quad (4)$$

where ε_{ext} is the external coupling strength and $g^{j,k}$ are the human brain matrix elements depicted in Fig. 2(a) for a healthy brain and in Fig. 2(b) for Alzheimer-affected brains [17]. In Figs. 2(a) and 2(b) white pixels represent the absence of connection between the ith and jth subnetworks leading to $g^{i,j} = 0$. Yellow, blue, and red pixels denote connection factors of $g^{i,j} = 1$, $g^{i,j} = 2$, and $g^{i,j} = 3$, respectively [17]. $\overline{V}_t^k$ is the mean field of each subnetwork k,

$$\overline{V}_t^k = \frac{1}{N} \sum_{i=1}^{N} x_{t,i}^k. \quad (5)$$

In a similar way, the mean field of the entire network is defined as

$$\overline{V}_{\text{global},t} = \frac{1}{NM} \sum_{j=1}^{M} \sum_{i=1}^{N} x_{t,i}^j. \quad (6)$$

Each subnetwork follows small-world properties considering a second neighborhood regular network and nonlocal connections with a probability $p = 0.0035$ [23]. The total number of connections of each subnetwork is given by

$$n = \underbrace{4N}_{\text{local}} + \underbrace{N(N-5)p}_{\text{nonlocal}}, \quad (7)$$

where $p = 1$ leads to a globally connected network.

III. THE KURAMOTO ORDER PARAMETER AND RECURRENCE QUANTIFICATION ANALYSIS

Figure 1(b) depicts the dynamics of the y variable of the neuron map. The local maximum of y coincides with the

starting of a burst in x dynamics, so a geometric phase for each neuron can be evaluated and the phase synchronization computed through the Kuramoto order parameter, since the phase is increased by 2π every time y assumes a local maximum. A continuous variation of phase for each neuron in the network is obtained by using linear interpolation [44]

$$\theta_i^j(t) = 2\pi k_i^j + 2\pi \frac{t - t_{k,i}^j}{t_{k+1,i}^j - t_{k,i}^j}, \quad t_{k,i}^j < t < t_{k+1,i}^j, \quad (8)$$

where $t_{k,i}^j$ is the time for which y assumes a local maximum and the kth burst of the ith neuron belonging to the jth network starts.

The Kuramoto order parameter for each network j is defined as [34]

$$R^j(t) = \left| \frac{1}{N} \sum_{k=1}^{N} e^{i\theta_k^j(t)} \right|, \quad (9)$$

and the global Kuramoto order parameter can be computed for the entire network as

$$R_{\text{global}}(t) = \left| \frac{1}{MN} \sum_{j=1}^{M} \sum_{k=1}^{N} e^{i\theta_k^j(t)} \right|. \quad (10)$$

To evaluate the intermittent behavior of the network, we employ determinism, a well-known tool of recurrence quantification analysis (RQA) [35]. The RQA is based on the original idea of the recurrence matrix, a graphical tool developed by Eckmann *et al.* [36]. A mathematical definition of the recurrence matrix is given by

$$\mathbf{R}_{ij}(\mu) = \Theta(\mu - ||\mathbf{w}_i - \mathbf{w}_j||), \mathbf{w}_i \in \mathbb{R}, \ i, j = 1, 2, \dots, S, \quad (11)$$

where μ is the recurrence threshold, S is the size of the time series, and Θ is the Heaviside function. So if a given state i is (not) recurrent to another state j, then the correspondent element of the matrix is set to a value 1 (zero).
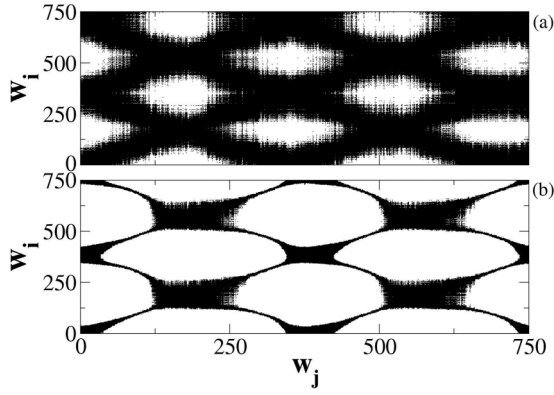
FIG. 3. Recurrence plot for an unsynchronized (a) and synchronized (b) networks. Observe that for case (b) the diagonal structures are clearer, suggesting Δ as a useful tool to diagnose the phase synchronization of networks.

Particularly important are the diagonal lines of the recurrence matrix formed by 1s, since the determinism (Δ) is measured as the ratio of recurrent points that belong to diagonal lines and all recurrent points on the recurrence matrix

$$\Delta(\ell_{min}, \mu) = \frac{\sum_{\ell=\ell_{min}}^{S} \ell P(\ell, \mu)}{\sum_{\ell=1}^{S} \ell P(\ell, \mu)}, \qquad (12)$$

where ℓ and ℓ_{min} are the lengths of diagonal lines and the minimum diagonal length considered. $P(\ell, \mu)$ is the probability distribution function (PDF) of diagonals lines.

The recurrence threshold μ is chosen from the condition that $d[\Delta(\mu)]/d\mu$ assumes a maximum, resulting in a more sensitive quantifier to analyze stationary changes in the time series [37]. To avoid small diagonals such that phase-synchronized and -unsynchronized states are better distinguishable, the minimum diagonal length considered is $l_{min} = 35$ [14]. Δ is evaluated using a moving window of 10 000 points and over the mean field of the entire system described by Eq. (6), turning it in an easier tool in comparison to other quantifiers that must be evaluated using information of each neuron in the network. These parameters are kept constant for all analyses.

To understand better why Δ can be used to quantify (un)synchronized states, Figs. 3(a) and 3(b) display the recurrence plots of the global mean-field representative of unsynchronized and synchronized networks, respectively. A phase-synchronized network has a higher oscillatory mean-field amplitude when compared to a nonsynchronized one. Using an optimized vicinity parameter [37], the determinism is able to capture the "periodic" behavior of the synchronized network mean field, as demonstrated by clearer diagonal lines in the recurrence plot, Fig. 3(b), leading to bigger values of Δ.

IV. RESULTS AND DISCUSSIONS

A. Phase synchronization

First, we focus on the general scenario of the synchronization level of the network as a function of internal and external coupling strengths. To quantify the transition to phase-synchronized states of each subnetwork, we use the mean

value in time $\langle \cdot \rangle$ of the Kuramoto order parameter, Eq. (9),

$$\langle R \rangle^j = \frac{1}{t_f - t_0} \sum_{t=t_0}^{t_f} R^j(t), \qquad (13)$$

where j is the specific subnetwork, $t_0 = 100\,000$ is the transient time, and $t_f = 150\,000$ is the total time considered. Accordingly, the average over all subnetworks of the mean value of the Kuramoto order parameter of each subnetwork is written as

$$\overline{\langle R \rangle} = \frac{1}{M} \sum_{j=1}^{M} \langle R \rangle^j. \qquad (14)$$

Similarly, the global mean value in time of the Kuramoto order parameter, Eq. (10), is

$$\langle R \rangle_{\text{global}} = \frac{1}{t_f - t_0} \sum_{t=t_0}^{t_f} R_{\text{global}}(t). \qquad (15)$$

We also define the difference between the average over all subnetworks of the mean value of the Kuramoto order parameter and the mean value of the global Kuramoto order parameter as [6]

$$\delta R = \overline{\langle R \rangle} - \langle R \rangle_{\text{global}}. \qquad (16)$$

Figure 4 depicts the results about the synchronization scenario of the networks. Figures 4(a) and 4(b) depict the mean value of the global Kuramoto order parameter [Eq. (15)] of the healthy and the Alzheimer-affected networks. A first comparison reveals visual differences between the healthy and unhealthy brain coupling matrices. For the healthy network [Fig. 4(a)], even for larger values of ε_{int} and ε_{ext}, just moderate levels of phase synchronization are observed and accordingly $\max\langle R \rangle_{\text{global}} \approx 0.75$. For the Alzheimer network [Fig. 4(b)], large values of ε_{int} and ε_{ext} result in $\max\langle R \rangle_{\text{global}} \approx 0.9$, suggesting a higher level of global phase synchronization.

Another important point consists of the behavior of the networks for $\varepsilon_{\text{ext}} < 0.25 \times 10^{-3}$. For the healthy one, a subtle transition from unsynchronized (dark tones) to partially phase-synchronized states (yellow tones) as ε_{ext} grows is observed. The level of phase synchronization is then smoothly increased as ε_{ext} increases. For the Alzheimer-affected network, the transition region spreads over a larger interval of ε_{ext} and strong levels of phase synchronization are found, even for small amplitudes, $\varepsilon_{\text{ext}} < 0.25 \times 10^{-3}$, as can be observed by the occurrence of pale yellow spots in Fig. 4(b), configuring a large region where intermittent phase synchronization is likely to occur. This scenario corroborates the idea that disruption on synchronized rhythms from slow δ range to ultrafast γ ranges may be related to neurological conditions, including brain trauma, schizophrenia, and Alzheimer's disease processes [21]. The literature reports that disruptions of γ-collective oscillations might contribute to the accumulation of amyloid-β protein in the brain—a hallmark of Alzheimer's disease [45]. Abnormal network activity in Alzheimer's disease is also provided by radiological studies, positron-emission tomography or single-photon-emission computed tomography, and magnetic resonance imaging [46–48]. These alterations may reflect the overall decreases in neuronal and synaptic activity but could also result from intermittent excesses in excitatory neuronal activity [46].
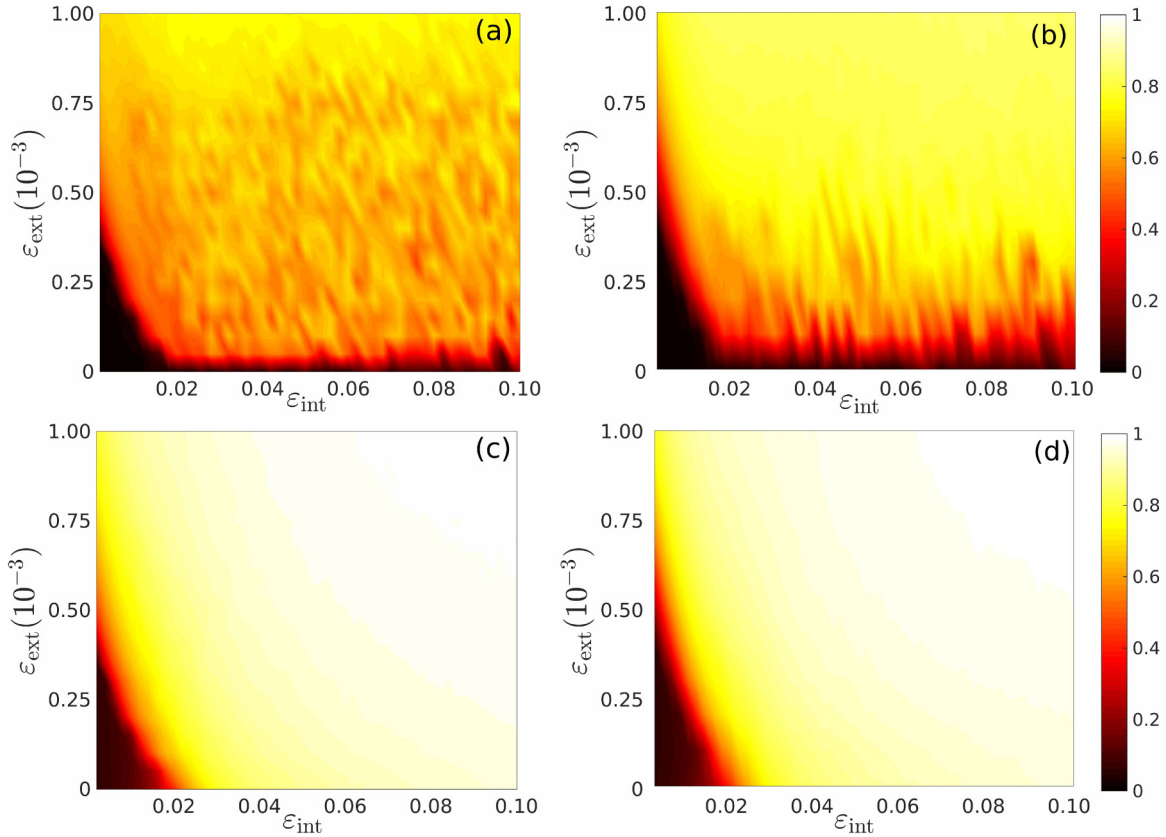
FIG. 4. Mean value of the Kuramoto order parameter as function of internal (ε_{int}) and external (ε_{ext}) coupling strengths. High mean values of the Kuramoto order parameter indicate high phase synchronization. Panels (a) and (b) depict the mean value of the global Kuramoto order parameter [Eq. (15)] for healthy and Alzheimer-affected networks. Note the higher levels of phase synchronization for the unhealthy network. Panels (c) and (d) depict the average of the Kuramoto order parameter over all subnetworks. Despite the distinct global behavior of the networks, the internal phase synchronization of each subnetwork is very similar.

The scenario is completely different when the individual behavior (local level) of each subnetwork is considered since the pathological concentration of naturally secreted oligomers of amyloid-β trigger aberrant patterns of neuronal circuit activity and epileptiform discharges at the network level [46]. Figures 4(c) and 4(d) depict the average of the mean value of the Kuramoto order parameter of each subnetwork [Eq. (14)]. Independently of healthy or unhealthy networks, the transition to phase-synchronized states of each subnetwork occurs in a very similar way. Note that $\overline{\langle R \rangle} \rightarrow 1$ for relatively small values of ε_{ext} and/or ε_{int}, showing that all subnetworks acquire the internal phase synchronization but for almost all phase space considered the subnetworks are not synchronized with each other. An important point emerges from the analyses of Figs. 4(a)–4(d), the major levels of globally phase synchronization (phase-synchronized subnetwork) for large ε_{ext} and a more significant intermittent region for low values of ε_{ext} are artifacts of the Alzheimer-affected network connection matrix. The results of Fig. 4 suggest that Alzheimer's disease makes subnetworks more susceptible to display intermittent phase-synchronized dynamics for low-ε_{ext} regimes.

A quantitative method to observe the difference between global phase synchronization and the subnetwork internal phase synchronization is given by δR, defined by Eq. (16).

Results for δR are depicted in Fig. 5(a) for the healthy network and in Fig. 5(b) for the unhealthy one. When each subnetwork is individually phase synchronized but not synchronized to each other, the entire network will be desynchronized and $\delta R \approx 1$. This behavior is clearly observed for the regime of weak ε_{ext} and strong ε_{int}, resulting in the pale red and yellow tones observed at the bottom of Figs. 5(a) and 5(b). All other features of Fig. 5 must be discussed in association with Fig. 4 since a globally phase-synchronized or -unsynchronized network results in $\delta R \approx 0$. Dark tones associated with small values of ε_{int} and ε_{ext}, as observed in both panels, result from the completely unsynchronized subnetworks due to small couplings. On the other hand, the overall dark red tones observed in Fig. 5(b) show that Alzheimer-affected networks reach an almost completely globally phase-synchronized network. This feature is absent in healthy networks, which never display global phase synchronization for the same interval of ε_{int} and ε_{ext}.

The results obtained so far have used the individual signals of each neuron of the network. However, important features of the network dynamics can be obtained using just the mean field of the entire network, described by Eq. (6). To do so, we make use of recurrence quantification analysis [13,14,37]; namely, we compute the determinism described by Eq. (12) for the healthy and Alzheimer networks.
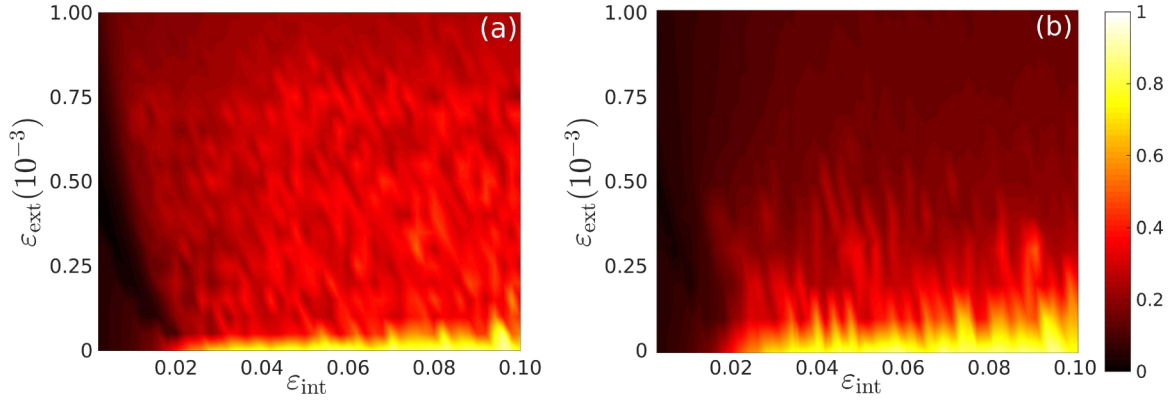
FIG. 5. Differences between the global Kuramoto order parameter, Eq. (15), and mean values of all subnetwork Kuramoto order parameters, Eq. (14). High mean values of the δR indicate high phase synchronization of subnetworks but absence of global phase synchronization. (a) A healthy network. (b) Alzheimer network. The healthy network presents larger values of δR, indicating a bigger difference between the entire synchronization behavior of the network and the mean internal subnetwork synchronization behavior.

The standard deviation of the time series of the windowed computed determinism Δ,

$$\sigma(\Delta) = \sqrt{\frac{1}{T} \sum_{i=1}^{T} [\Delta(i) - \langle \Delta \rangle]^2},\qquad(17)$$

can be used to investigate the dynamical properties of the network since the individual synchronized subnetwork and the globally phase-synchronized network result in distinct values for $\sigma(\Delta)$. Moreover, another important feature of the recurrence analysis is the clear distinction of the transition regions from the unsynchronized network, individually phase-synchronized subnetwork, and globally phase-synchronized network [14]. Since Δ distinguishes between synchronized and nonsynchronized states displaying distinct mean values [14], the temporal standard deviation of Δ can be used to get information about the intermittent behavior of the neural system. As long as Δ displays stationary oscillations around a fixed value, $\sigma(\Delta)$ will display a low value. For an intermittent behavior of the windowed computed Δ, large oscillations of $\sigma(\Delta)$ are expected, such that it can be used to characterize intermittency of the time series. The results provided by $\sigma(\Delta)$ lead to a similar scenario to the one described by the difference of the order parameter, as depicted in Fig. 5, but making use only of the network mean field.

Figures 6(a) and 6(b) depict $\sigma(\Delta)$ of the windowed computed determinism based on time series (length of 10^6 points) of the mean field of the network, Eq. (6), as a function of ε_{int} and ε_{ext} for the healthy [Fig. 6(a)] and Alzheimer-affected [Fig. 6(b)] networks. As already observed in Figs. 5(a) and 5(b), individually phase-synchronized subnetworks are observed for low values of the ε_{ext} and high values of the ε_{int}. Results based on $\sigma(\Delta)$, namely its large dispersion in time in the region of individual subnetwork phase synchronization, lead us to conclude that the global dynamics is intermittent. Such an intermittent behavior must come from the nonperennial clustering synchronization of the subnetworks. The unsynchronized regime for low values of both couplings results into small values of $\sigma(\Delta)$, revealing that for the unsynchronized regime of the network, all subnetworks

evolve in a similar stationary dynamics. The transition from a completely unsynchronized regime to the partially global phase-synchronized network occurs via an increase of $\sigma(\Delta)$, suggesting again an intermittent (nonstationary) transition, as observed in other networks [13,14]. Finally, for large values of both coupling parameters, a relatively stationary behavior of all subnetworks can be inferred since $\sigma(\Delta)$ oscillates around a very low value.

B. Intermittent transition to phase synchronization

To explore the details of the intermittent characteristics of the transition to global phase synchronization depicted by the healthy and unhealthy connectome brain matrices, Figs. 7(a)–7(f) depict the normalized PDFs of six representative regions as defined in Fig. 6. The PDFs are computed for the windowed determinism of the global mean field of the networks of healthy (black dashed lines) and Alzheimer-affected (red solid lines) networks.

Figure 7(a) depicts PDFs of the unsynchronized states of both networks, region (1) in Fig. 6. Narrow distributions reveal the stationary characteristic of the dynamics of both networks. Figure 7(b) shows results for region (2) in Fig. 6, a transition region characterized by small values of both couplings. A clear intermittent characteristic of the transition is evident. The two peaks of both distributions are related to the presence of two distinct states, characterized by different levels of phase synchronization. The networks stay shifting between these two states, suggesting a local stability but a global instability of the network dynamics [13,14].

Figure 7(c) is representative of a region of intermediate values of ε_{int} and weak values of ε_{ext}. Once again the intermittent characteristic is evident but only for the Alzheimer-affected (red solid lines) networks. These results suggest that Alzheimer-affected connectomes demand higher values of ε_{ext} to shift from individual subnetwork phase synchronization to partially global phase-synchronized states. This behavior of the Alzheimer-affected networks corroborates the experimental evidence that the Alzheimer connectome still behaves as a small-world matrix but exhibits higher shortest path lengths [17], evidencing the loss of connections between brain areas.
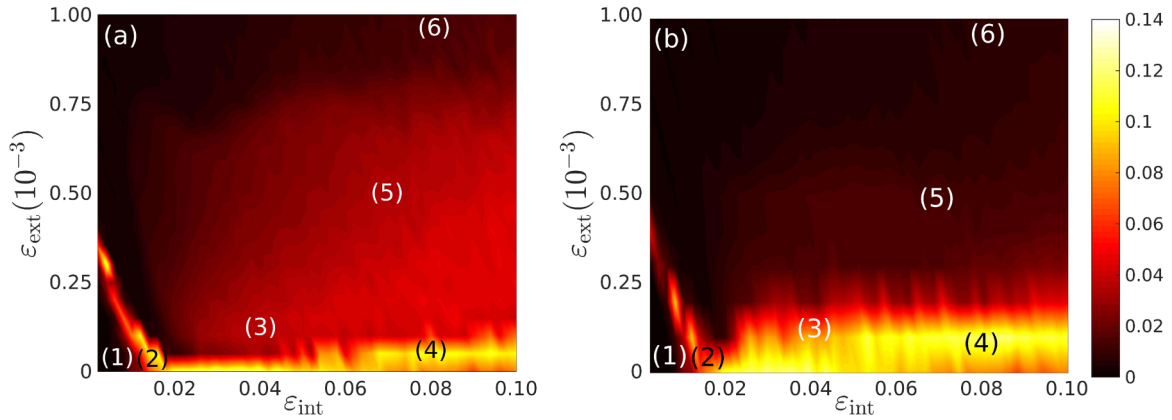
FIG. 6. Color-coded standard deviation of the windowed determinism time series of the network mean field as a function of ε_{int} and ε_{ext} coupling strengths. High mean values of $\sigma(\Delta)$ are an indication of intermittency regions of the parameter space. Panel (a) shows a healthy network while panel (b) shows an unhealthy one. The intermittent transition areas are clearly observed as pale red, yellow, and pale yellow tones. Selected areas (1)–(6) are analyzed in Fig. 7.

More than that, it reinforces the observation that Alzheimer's disease is characterized as a functional network disorder [22]. A representative distribution of the region of strong ε_{int} and weak ε_{ext} is depicted in Fig. 7(d). In this case, common characteristics between healthy and unhealthy connectomes reveal a moderate level of intermittency at the transition from individual subnetwork phase synchronization to a partially global phase synchronization. Figure 7(e) is representative of a moderated ε_{ext} amplitude. For this case the unhealthy connectome shows a higher level of global phase synchronization, suggesting an abnormal stationary and globally synchronized

state, occurring even for moderated ε_{ext} strengths (a higher value of Δ indicates a higher synchronization of the signal, corroborating the previously synchronization analysis). Finally, Fig. 7(f) just reveals the case of an asymptotic global phase-synchronized and stationary state depicted by both networks. Note the higher mean value of Δ pointing out the higher phase synchronization of the unhealthy network.

Figure 8 displays examples of time series of the windowed computed determinism of the mean field of both networks. Figures 8(a) and 8(b) show typical determinism signals for unsynchronized and stationary states, $\varepsilon_{int} = 0.007$, $\varepsilon_{ext} =$
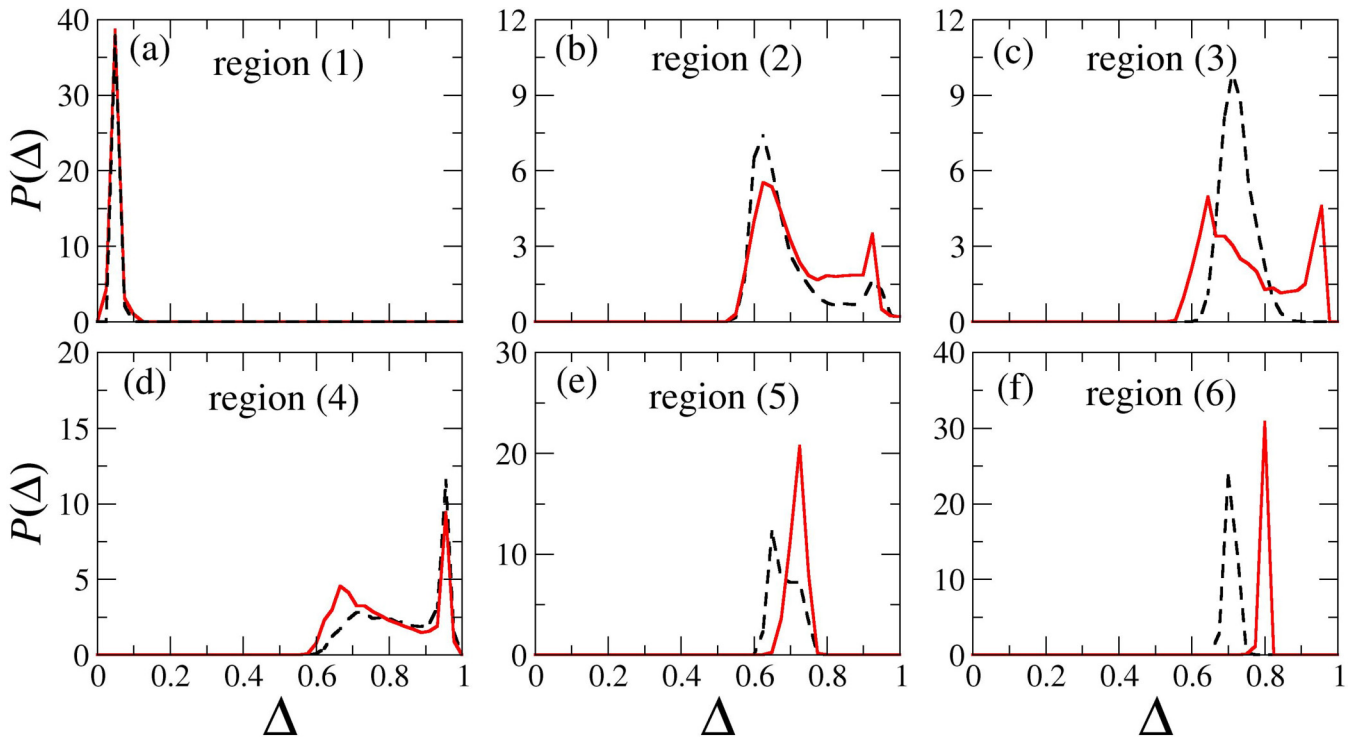

FIG. 7. Normalized PDFs of the windowed determinism time series of the mean-field potential of the entire network for healthy (black dashed lines) and Alzheimer (red solid lines) connectomes. Regions (1)–(6) are identified in Fig. 6 and coupling parameters are (a) $\varepsilon_{ext} = 0.05 \times 10^{-3}$ and $\varepsilon_{int} = 0.007$, (b) $\varepsilon_{ext} = 0.05 \times 10^{-3}$ and $\varepsilon_{int} = 0.015$, (c) $\varepsilon_{ext} = 0.12 \times 10^{-3}$ and $\varepsilon_{int} = 0.040$, (d) $\varepsilon_{ext} = 0.10 \times 10^{-3}$ and $\varepsilon_{int} = 0.080$, (e) $\varepsilon_{ext} = 0.50 \times 10^{-3}$ and $\varepsilon_{int} = 0.070$, and (f) $\varepsilon_{ext} = 1.00 \times 10^{-3}$ and $\varepsilon_{int} = 0.080$.
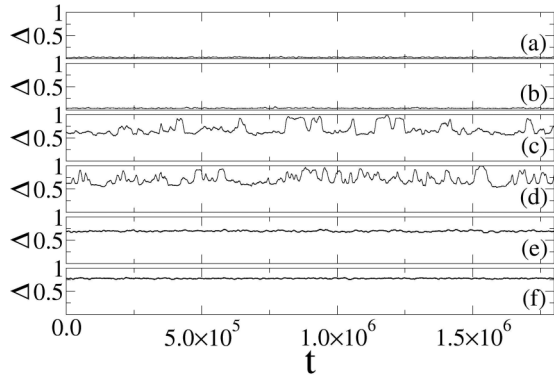
FIG. 8. Time series of the windowed computed determinism. Panels (a) and (b) depict the globally stable unsynchronized case [$\varepsilon_{ext} = 0.05 \times 10^{-3}$ and $\varepsilon_{int} = 0.007$ region (1) on Fig. 6] for healthy and Alzheimer-affected networks. Panels (c) and (d) display a two-state intermittency case [$\varepsilon_{ext} = 0.05 \times 10^{-3}$ and $\varepsilon_{int} = 0.015$ region (2) on Fig. 6] for healthy and unhealthy networks. Panels (e) and (f) show a global stable phase-synchronized case [$\varepsilon_{ext} = 1.00 \times 10^{-3}$ and $\varepsilon_{int} = 0.080$ region (6) on Fig. 6] for healthy and unhealthy networks.

0.05×10^{-3} [region (1) as depicted in Fig. 6] for healthy and Alzheimer networks. Figures 8(c) and 8(d) depict typical intermittent determinism signals for $\varepsilon_{int} = 0.015$ and $\varepsilon_{ext} = 0.05 \times 10^{-3}$ [region (2) as depicted in Fig. 6], where Δ clearly oscillates around two distinct values. Last, Figs. 8(e) and 8(f) show the global stable phase-synchronized states occurring for $\varepsilon_{int} = 0.80$ and $\varepsilon_{ext} = 1.00 \times 10^{-3}$ [region (6) as depicted in Fig. 6].

Further details about the dynamical process that allows the shifting between the two states observed for the networks and shown in Figs. 7 and 8 can be attained using the PDFs of the time intervals (τ) where the networks spend in each

particular state, leading to higher and lower values of Δ. The results are depicted in Figs. 9(a)–9(d) and suggest that the windowed determinism is sensitive enough to evaluate different dynamical states shown by the networks.

Figures 9(a) and 9(b) depict the PDFs of the laminar time periods where the healthy network spends in a less-synchronized state [the lower state; Fig. 9(a)], and in the more globally phase-synchronized state [upper state; Fig. 9(b)], while Figs. 9(c) and 9(d) depict the same analysis but for the Alzheimer-affected network. For both cases, $\varepsilon_{ext} = 0.05 \times 10^{-3}$ and $\varepsilon_{int} = 0.015$ [region (2)] in Figs. 6 and 7(b) are considered. Power-law -scaling PDFs for the smaller laminar periods associated with an exponential distribution for large intervals of time are observed. The exponential scales for large intervals are expected due to intrinsic noise in the simulation that does not allow large intervals of time in a specific dynamical state.

A similar scenario was found in other neural systems [12–14] and in turbulent regimes [49] and they have been explained in terms of two-state on-off intermittency [50]. In this scenario, two locally stable but globally unstable asymptotic states are present in the dynamics, such that the network dynamics can be classified as nonstationary and the transition from unsynchronized to phase-synchronized states are characterized as an out-of-equilibrium transition. As the coupling parameter is varied, the global stability of the lower branch of the dynamics is lost, turning it in just a locally stable state. Further increase of the coupling allows a transition region where locally stable and globally unstable lower and higher phase-synchronization states exist. For high values of the coupling parameter, the transition region vanishes, giving rise to a globally stable phase-synchronized state and the intermittent scenario is replaced by globally stable and stationary states, as depicted in Fig. 7(f). A similar scenario of network intermittent mean-field dynamics is associated to
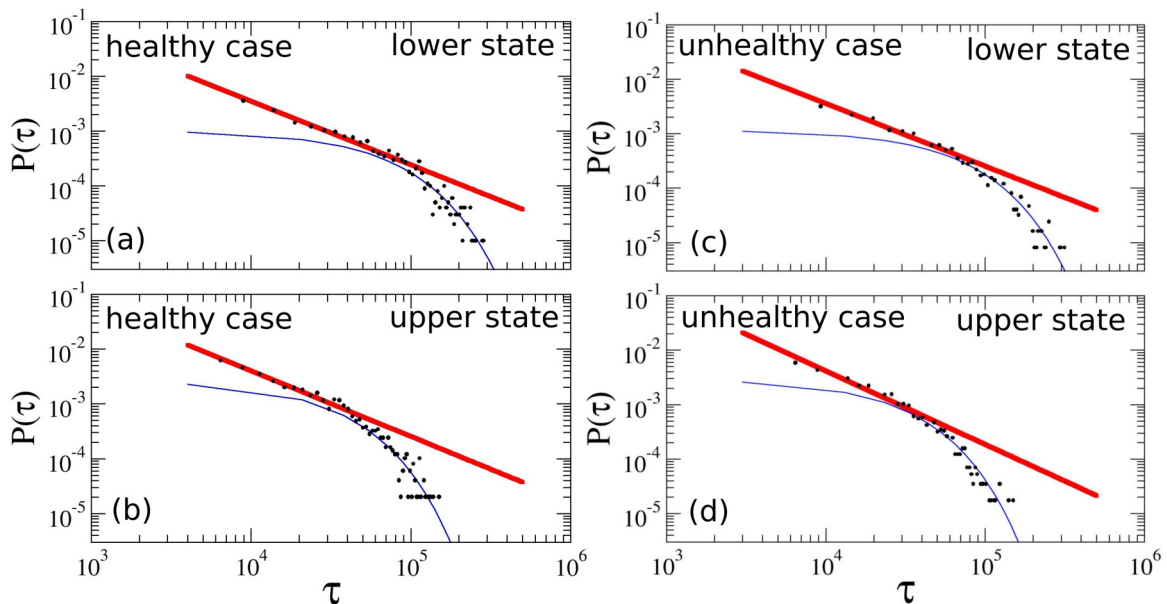

FIG. 9. Normalized PDF of laminar periods for which the networks stay in each intermittent state (characterized by two peaks in determinism distribution) depicted in Fig. 7(b) for healthy and unhealthy networks. Thick red lines are power-law fitting. (a) $P(\tau) \propto \tau^{-1.16}$, (b) $P(\tau) \propto \tau^{-1.17}$, (c) $P(\tau) \propto \tau^{-1.10}$, and (d) $P(\tau) \propto \tau^{-1.18}$. The thin blue lines represent exponential fits.

the behavior of neural synchronization in Alzheimer's disease, where abnormal disruptions of γ oscillations are reported to be common and, in general, associated to the presence of amyloid-β protein, a hallmark of Alzheimer's disease [21].

V. CONCLUSION

We have studied the dynamical properties of a neural system composed of a network of networks based on human health and Alzheimer-affected brains. The neural systems were composed of 78 subnetworks representative of the cortical areas and coupled by experimentally obtained connectomes of Alzheimer-affected and healthy patients, as described by Lo *et al.* [17].

We have identified distinct characteristics of the dynamical properties of healthy and unhealthy networks, regarding the global phase-synchronization transition, intermittency, and local and global stabilities of the asymptotic states of both cases. The subnetworks are internally coupled through a similar small-world connection scheme since real networks displaying such a topology are reported [2,24,25]. The internal dynamics of each subnetwork is considered to be composed of 250 nonidentical bursting neurons.

By using the Kuramoto order parameter [34], we have demonstrated that the unhealthy neural networks reach a higher level of global phase synchronization in comparison to the healthy cases, which is an interesting observation, since some neural diseases are associated with excess of synchronization, as observed in Refs. [31,32,51,52].

Through recurrence quantification analysis, particularly determinism [35], we have identified distinct behaviors regarding the intermittency characteristics of the transition to the global phase synchronization of healthy and Alzheimer-affected networks. Unhealthy cases reach a higher level of intermittency in a relatively large interval of ε_{ext}. Despite the large intermittent regime occurring as the ε_{ext} grows, Alzheimer-affected networks rapidly reach a stronger global phase-synchronized state, occurring even for relatively small ε_{ext}.

Healthy networks present a much smoother transition to global phase synchronization as the ε_{ext} is increased. The global level of phase synchronization is lower than those observed for the Alzheimer networks. In this way, the distinct dynamical characteristics found here can help the understanding of dynamical details of neural systems related to the intermittent behavior and associated with neural dysfunctions [33].

This scenario may be related to the idea that intermittent disruption on synchronized rhythms of several brain rhythms may be related to neurological conditions, including Alzheimer's disease processes [21]. In fact, disruptions of γ-collective oscillations might contribute to the accumulation of amyloid-β protein in the brain—a well-known signature of Alzheimer's disease [45].

Despite the differences found between the healthy and Alzheimer networks, a common characteristic of both cases consists of the fact that the transition regions present nonstationarity behavior, where we identify sets of coupling parameters in which the system displays two-state on-off intermittency [49], where asymptotic states display local stability but global instability, allowing the networks to show perennial shifting between two distinct short-time characteristic trajectories. Similar results found in other neural systems demonstrate this recurrent phenomenon in the transition from unsynchronized states to globally phase-synchronized ones [12–14].

Last, we emphasize that the use of the Kuramoto order parameter demands data of each neuron of the networks, while the determinism is computed over the mean-field potential of the entire network, which is more easily accessible in most real situations, where, in general, information for each neuron is not available. This fact demonstrates that recurrence analysis may be used as a useful tool to analyze dynamical properties and, as observed in Refs. [53–55], to be able to evaluate data from experimental systems.

[1] E. R. Kandel, J. H. Schwartz, T. M. Jessell, S. A. Siegelbaum, A. J. Hudspeth *et al.*, *Principles of Neural Science*, Vol. 4 (McGraw–Hill, New York, 2000).

[2] L. R. Varshney, B. L. Chen, E. Paniagua, D. H. Hall, and D. B. Chklovskii, PLoS Comput. Biol. **7**, e1001066 (2011).

[3] C. C. Hilgetag and M. Kaiser, *Lectures in Supercomputational Neuroscience: Dynamics in Complex Brain Networks*, edited by P. B. Grabe, C. Zhou, M. Thiel, and J. Kurths (Springer, Berlin, 2008).

[4] E. Bullmore and O. Sporns, Nat. Rev. Neurosci. **10**, 186 (2009).

[5] F. A. S. Ferrari, R. L. Viana, A. S. Reis, K. C. Iarosz, I. L. Caldas, and A. M. Batista, Physica A **496**, 162 (2018).

[6] T. de L. Prado, S. R. Lopes, C. A. S. Batista, J. Kurths, and R. L. Viana, Phys. Rev. E **90**, 032818 (2014).

[7] E. L. Lameu, C. A. S. Batista, A. M. Batista, K. Iarosz, R. L. Viana, S. R. Lopes, and J. Kurths, Chaos **22**, 043149 (2012).

[8] S. H. Strogatz, Nature **410**, 268 (2001).

[9] Y. Bar-Yam, *Dynamics of Complex Systems* (Addison-Wesley, Reading, MA, 1997).

[10] N. Boccara, *Modeling Complex Systems* (Springer Science & Business Media, Berlin, 2010).

[11] S. Stramaglia, M. Pellicoro, L. Angelini, E. Amico, H. Aerts, J. Cortés, S. Laureys, and D. Marinazzo, Chaos **27**, 047407 (2017).

[12] B. R. R. Boaretto, R. C. Budzinski, T. L. Prado, J. Kurths, and S. R. Lopes, Physica A **497**, 126 (2018).

[13] R. C. Budzinski, B. R. R. Boaretto, T. L. Prado, and S. R. Lopes, Phys. Rev. E **96**, 012320 (2017).

[14] R. C. Budzinski, B. R. R. Boaretto, K. L. Rossi, T. L. Prado, J. Kurths, and S. R. Lopes, Physica A **507**, 321 (2018).

[15] K. Xu, J. P. Maidana, S. Castro, and P. Orio, Sci. Rep. **8**, 8370 (2018).

[16] B. R. R. Boaretto, R. C. Budzinski, T. L. Prado, J. Kurths, and S. R. Lopes, Chaos **28**, 106304 (2018).

[17] C.-Y. Lo, P.-N. Wang, K.-H. Chou, J. Wang, Y. He, and C.-P. Lin, J. Neurosci. **30**, 16876 (2010).

[18] C. Pierpaoli, P. Jezzard, P. J. Basser, A. Barnett, and G. Di Chiro, Radiology **201**, 637 (1996).

[19] F. Christidi, E. Karavasilis, K. Samiotis, S. Bisdas, and N. Papanikolaou, Eur. J. Radiol. **3**, 153 (2016).

[20] H. Aerts, W. Fias, K. Caeyenberghs, and D. Marinazzo, Brain **139**, 3063 (2016).

[21] L. Aron and B. A. Yankner, Nature **540**, 207 (2016).

[22] W. de Haan, W. van der Flier, T. Koene, L. Smits, P. Scheltens, and C. Stam, NeuroImage **59**, 3085 (2012).

[23] M. E. J. Newman and D. J. Watts, Phys. Rev. E **60**, 7332 (1999).

[24] Y. He, Z. J. Chen, and A. C. Evans, Cereb. Cortex **17**, 2407 (2007).

[25] C. J. Stam and E. C. W. Van Straaten, Clin. Neurophysiol. **123**, 1067 (2012).

[26] C. A. S. Batista, E. L. Lameu, A. M. Batista, S. R. Lopes, T. Pereira, G. Zamora-López, J. Kurths, and R. L. Viana, Phys. Rev. E **86**, 016211 (2012).

[27] D. J. Watts and S. H. Strogatz, Nature **393**, 440 (1998).

[28] H. Bi, X. Hu, S. Boccaletti, X. Wang, Y. Zou, Z. Liu, and S. Guan, Phys. Rev. Lett. **117**, 204101 (2016).

[29] G. Deco, V. K. Jirsa, and A. R. McIntosh, Nat. Rev. Neurosci. **12**, 43 (2011).

[30] D. Papo, J. Goñi, and J. M. Buldú, Chaos **27**, 047201 (2017).

[31] A. Galvan and T. Wichmann, Clin. Neurophysiol. **119**, 1459 (2008).

[32] I. Dinstein, K. Pierce, L. Eyler, S. Solso, R. Malach, M. Behrmann, and E. Courchesne, Neuron **70**, 1218 (2011).

[33] L. D. Iasemidis and J. C. Sackellares, Neuroscientist **2**, 118 (1996).

[34] Y. Kuramoto, *Chemical Oscillations, Waves, and Turbulence*, Vol. 19 (Springer Science & Business Media, Berlin, 2012).

[35] N. Marwan, M. C. Romano, M. Thiel, and J. Kurths, Phys. Rep. **438**, 237 (2007).

[36] J. P. Eckmann, S. O. Kamphorst, and D. Ruelle, Europhys. Lett. **4**, 973 (1987).

[37] T. d. L. Prado, G. Z. dos Santos Lima, B. Lobão-Soares, G. C. do Nascimento, G. Corso, J. Fontenele-Araujo, J. Kurths, and S. R. Lopes, Chaos **28**, 085703 (2018).

[38] N. F. Rulkov, Phys. Rev. E **65**, 041922 (2002).

[39] N. F. Rulkov, Phys. Rev. Lett. **86**, 183 (2001).

[40] S. Coombes and P. C. Bressloff, *Bursting: The Genesis of Rhythm in the Nervous System* (World Scientific, Singapore, 2005).

[41] U. Feudel, A. Neiman, X. Pei, W. Wojtenek, H. A. Braun, M. Huber, and F. Moss, Chaos **10**, 231 (2000).

[42] H. A. Braun, M. Dewald, K. Schäfer, K. Voigt, X. Pei, K. Dolan, and F. Moss, J. Comput. Neurosci. **7**, 17 (1999).

[43] K. Schäfer, H. A. Braun, R. C. Peters, and F. Bretschneider, Pflüg. Arch. **429**, 378 (1995).

[44] M. V. Ivanchenko, G. V. Osipov, V. D. Shalfeev, and J. Kurths, Phys. Rev. Lett. **93**, 134101 (2004).

[45] H. F. Iaccarino, A. C. Singer, A. J. Martorell, A. Rudenko, F. Gao, T. Z. Gillingham, H. Mathys, J. Seo, O. Kritskiy, F. Abdurrob, C. Adaikkan, R. G. Canter, R. Rueda, E. N. Brown, E. S. Boyden, and L.-H. Tsai, Nature **540**, 230 (2016).

[46] J. J. Palop and L. Mucke, Nat. Neurosci. **13**, 812 (2010).

[47] G. B. Frisoni, M. Pievani, C. Testa, F. Sabattoli, L. Bresciani, M. Bonetti, A. Beltramello, K. M. Hayashi, A. W. Toga, and P. M. Thompson, Brain **130**, 720 (2007).

[48] R. L. Buckner, A. Z. Snyder, B. J. Shannon, G. LaRossa, R. Sachs, A. F. Fotenos, Y. I. Sheline, W. E. Klunk, C. A. Mathis, J. C. Morris *et al.*, J. Neurosci. **25**, 7709 (2005).

[49] P. P. Galuzio, S. R. Lopes, and R. L. Viana, Phys. Rev. E **84**, 056211 (2011).

[50] P. P. Galuzio, S. R. Lopes, and R. L. Viana, Phys. Rev. Lett. **105**, 055001 (2010).

[51] F. Mormann, K. Lehnertz, P. David, and C. E. Elger, Physica D **144**, 358 (2000).

[52] C. Hammond, H. Bergman, and P. Brown, Trends Neurosci. **30**, 357 (2007).

[53] G. Z. S. Lima, S. R. Lopes, T. L. Prado, B. Lobao-Soares, G. C. do Nascimento, J. Fontenele-Araujo, and G. Corso, PloS One **12**, e0176761 (2017).

[54] G. Corso, T. d. L. Prado, G. Z. S. Lima, J. Kurths, and S. R. Lopes, Chaos **28**, 083108 (2018).

[55] F. M. Neves, R. L. Viana, and M. R. Pie, PloS one **12**, e0185968 (2017).

Correction: Figures 2, 4–7, and 9 and captions to Figs. 2 and 9 contained errors and have been replaced. The omission of an acknowledgment statement has been remedied. The second complete sentence after Eq. (4) contained an error and has been fixed.